Proceedings of 39th International Conference on Ocean, Offshore, and Arctic Engineering
OMAE 2020
June 28–July 3, 2020, Fort Lauderdale, FL, USA

OMAE2020-19054

NUMERICAL MODEL DEVELOPMENT OF A VARIABLE-GEOMETRY ATTENUATOR WAVE ENERGY CONVERTER

Davy Pardonner
University of West Florida
Pensacola, FL USA
Email: davypardonner@gmail.com

Nathan Tom*
National Renewable
Energy Laboratory
Golden, CO USA
Email: Nathan.Tom@nrel.gov

Yi Guo
National Renewable
Energy Laboratory
Golden, CO USA
Email: Yi.Guo@nrel.gov

ABSTRACT

Because the wave energy industry is still in its infancy, an optimal design for wave energy converters (WECs) has yet to be established; more work is needed to explore various cost-reduction pathways. The primary cost-reduction pathway considered for this work is the optimization of the geometric profile on an attenuator WEC to maximize power production while, at the same time, minimizing capital expenditures through the use of variable-geometry modules. In this investigation, the variable-geometry modules consist of inflatable bags placed on either side of a base central steel cylinder that would be inflated in low-moderate sea states to maximize power capture and then deflated in moderate-extreme sea states to minimize wave loading. The numerical model and simulation of the attenuator WEC were developed and completed using WEC-Sim, which is an open-source code that is appropriate for use in evaluating the dynamic response of the different WEC models in operational seas. The power production estimates were obtained from the Wave Energy Prize (WEP) sea states, which are representative of U. S. deployment sites, to calculate the average climate capture width that is used in the WEP ACE calculation. Preliminary capital expenditure costs were obtained assuming the base central steel cylinder mass was equal to the fluid displaced mass, minus the mass of the variable-geometry bags. The additional weight required to offset the additional buoyancy from the variable-geometry bags was assumed to come from the addition of seawater ballast. The variable-geometry attenuator model was found to have a similar power capture efficiency as a fixed-body model, but is expected to have a lower characteristic capital expenditure given its more streamlined profile, which demonstrates that variable-geometry modules may provide a realistic cost-reduction pathway to help design a more cost-competitive WEC.

INTRODUCTION

The global resource of wave energy potential is estimated to be around 30,660 TWh/yr [1]; however, despite the large amount of potential energy available, the wave energy industry remains in the early stages of development and lacks a well-established wave energy converter (WEC) design. Over the past two decades, the global marine and hydrokinetic energy sector has experienced a resurgence in the funding and manpower allocated toward research and development. As a whole, the field of wave energy continues to host a wide diversity of technologies, ranging from concept- to prototype-scale devices [2]. However, the cost of energy for WECs remains at the high end of renewable energy technologies, highlighting the need for a structured, innovative approach to WEC development in hope of achieving an optimal convergence in technologies [3]. As shown in the U.S. Department of Energy Reference Model Project [4], the structural cost of WEC designs accounts for approximately 37–52% of the levelized cost of energy (LCOE), whereas the power take-off (PTO) is expected to contribute around 8% of LCOE [5]. Therefore, to make a significant impact on LCOE, structural design optimizations must be explored; however, these reductions will not be obtained until there is a greater load-shedding capability designed into the WEC structure. Recent work has attempted

*Address all correspondence to this author.

to incorporate variable-geometry modules into the structural design in hope of providing greater control over the hydrodynamic properties of the device that define power absorption and structural loading [6].

This study focuses on the hydrodynamic design of an attenuator WEC, which is generally characterized as a floating device that operates parallel to the wave direction and captures wave energy from the relative motion between two or more oscillating bodies. There have been several attenuator concepts previously explored, with select prototypes built and tested in the open ocean, such as the Pelamis Wave Power's P2 devices [7], Crestwing Tordenskiold [8], and the Dexa WEC [9]. Pelamis Wave Power had the first operational commercial WEC farm, which was deployed off the coast of Portugal starting in 2009. In 2019, Mocean Energy was awarded Wave Energy Scotland's Novel Wave Energy Converter Stage 3 funding to build and deploy a prototype of their Blue Star attenuator WEC [10]. Given the academic and commercial interest in the attenuator WEC concept, the WEC design for this study was modeled after the first-generation Pelamis design.

The goal of this study is to identify properties of a variable-geometry attenuator WEC that could potentially lead to a cost-competitive design for the wave energy industry. Incorporating variable-geometry components is expected to help improve the power capture efficiency in low-to-moderate sea states while capping power capture and reducing structural loads in large-to-extreme sea states. Improving power capture, while at the same time reducing costs, is expected to help provide significant reductions in LCOE rather than focusing solely on power maximization. In this work, the variable-geometry components will be flexible bags that are placed on either side of the main WEC body and can be inflated or deflated to alter the device profile in the water. This concept is similar to the Wave Energy Scotland novel wave energy converter proposed by Quocent [11] which demonstrated LCOE reductions of up to 50% using inflatables to control the hull volume. The use of flexible materials in the field of wave energy has also recently gained more attention because plastic or fabric bags are cheaper to manufacture, transport, and assemble, although there are additional hydrodynamic modeling challenges that must be considered [12].

This paper begins with a description of the base design of the attenuator WEC, its mass properties, and hydrostatic restoring forces that keep the absorber bodies floating at the sea surface. The paper then discusses how the hydrodynamic coefficients are affected by changing the primary dimensions of the idealized WEC structure in hope of identifying which geometrical dimensions play a greater role in power absorption and load accumulation. After discussing the WEC hydrodynamics, the paper introduces the WEC-Sim code, used to simulate the attenuator dynamics, and the sea states chosen to estimate the WEC power performance. Next, the variable-geometry flexible bag concept is introduced, followed by a discussion of the effects of the variable-geometry modules on the hull hydrodynamics. The variable-geometry module description is followed by an introduction to the ACE calculation [13], which is a simplified power-to-cost ratio that will be used to evaluate the overall performance of the variable-geometry WEC concept. The paper concludes with a discussion about the success of the attenuator WEC variable-geometry modules at improving power capture while reducing the capital costs related to the device structural design.

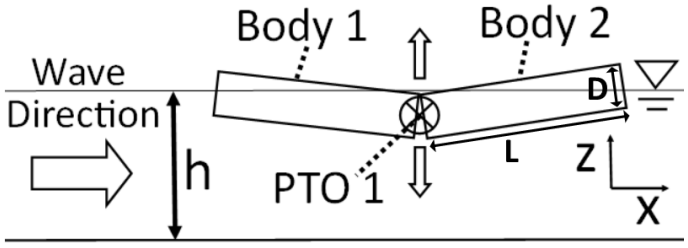

FIGURE 1. SCHEMATIC OF THE TWO-BODY ATTENUATOR WEC-SIM MODEL, INCLUDING THE FREE SURFACE, WAVE DIRECTION, BODY 1, BODY 2, AND PTO 1.

TWO-BODY MODEL DESCRIPTION

The two-body attenuator WEC consists of two identical floating cylindrical hulls with a rotational PTO connecting the two bodies, refer to Figure 1. The hull mass is assumed to be uniformly distributed, which sets the center of gravity at the geometric center of the body. The inertial properties of a single body, about the center of gravity, is defined by the following equations:

$$V_d = \frac{\pi D^2 L}{8},\ m = \rho \frac{\pi D^2 L}{8},\ I_{55} = \frac{mL^2}{12}\left[1 + \frac{3}{4}\left(\frac{D}{L}\right)^2\right], \quad (1)$$

$$z_b = [0, 0, \frac{-2D}{3\pi}],\ C_{33} = \rho g D L, \quad (2)$$

$$C_{55} = \rho g I_y + \rho g V_d z_b - m g z_g = \rho g \frac{DL^3}{12}\left[1 - \left(\frac{D}{L}\right)^2\right], \quad (3)$$

where V_d is the displaced volume of the cylinder, D is the diameter of the cylinder, L is the length of the cylinder, m is the mass of cylinder, ρ is the fluid density, I_{55} is the pitch mass moment of inertia of the cylinder, z_b is the vertical center of buoyancy, C_{33} is the heave hydrostatic restoring coefficient, C_{55} is the pitch hydrostatic restoring coefficient, I_y is the second moment of area of the water plane area, and z_g is the vertical center of gravity. Each body is designed to float with a draft equal to half the cylinder diameter, and with the mass of the body equal to the mass of the displaced fluid. The inertial and geometric properties of a single body are listed in Table 1. For comparison, the individual bodies

of the Pelamis P1 design had a length, L = 35 m, and diameter, D = 3.5 m [14]. The dimensions for our attenuator model were adjusted from the Pelamis P1 to better suit the wave conditions at U.S. deployment sites. For dynamic modeling purposes, the system was constrained to oscillate in the surge, heave, and pitch degrees of freedom (DOF) while the relative pitch rotation between the two bodies drove a rotary PTO to harvest wave power.

TABLE 1. BASE MASS AND GEOMETRIC DIMENSIONS FOR A SINGLE-BODY SEGMENT.

Variable	Symbol	Value [unit]
Length	L	25 [m]
Diameter	D	3 [m]
Draft	d	1.5 [m]
Displaced Volume	$\forall$	88.36 [m^3]
Mass	m	88357 [kg]
Pitch Mass Moment of Inertia	I_{55}	4.65×10^6 [kg$\cdot$ m^2]
Center of Gravity	c_g	0, 0, 0 [m]
Center of Buoyancy	c_b	0, 0, -0.636 [m]

WEC Hydrodynamics

The first step in this study was the examination of the hydrodynamic coefficients for different geometric hull shapes to help size the WEC. The surge, heave, and pitch hydrodynamic coefficients were calculated using WAMIT version 7.2 [15], at the center of gravity of each body, and were computed before the power performance and corresponding loading of the WEC could be estimated. Although the hydrodynamic coefficients for each DOF contribute to the relative pitch motion between the two bodies, only the heave hydrodynamic coefficients are discussed in this section (for brevity).

The length of each body was modeled at four values, in addition to the base case shown in Table 1, while keeping the diameter, D, constant at 3 m. The heave radiation added mass, μ_{33}, and wave damping, λ_{33}, for body 1 are plotted in Figure 2, with body 2 values omitted because the radiation problem is symmetric, resulting in the same values for each body. The radiation hydrodynamic coefficients have been nondimensionalized by the WEC mass which, in this case, scales linearly with body length. Therefore, in Figure 2, if the radiation coefficient curves were to lie on top of one another, the radiation coefficients would scale linearly with body length; however, at low wave frequencies, the

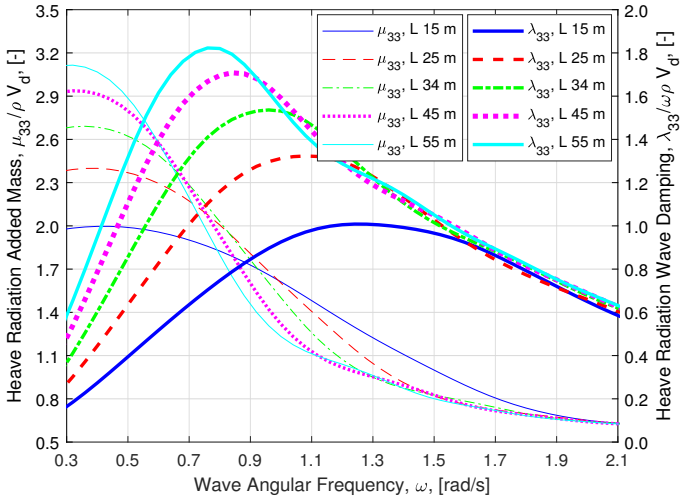

FIGURE 2. HEAVE RADIATION ADDED MASS, μ_{33}, AND WAVE DAMPING, λ_{33}, FOR EACH BODY 1 LENGTH. AS THE RADIATION PROBLEM IS SYMMETRIC, THE RADIATION COEFFICIENTS ARE IDENTICAL FOR BODY 2 AND ARE OMITTED.

heave-added mass grows nonlinearly as the body length is increased. In the intermediate frequency range, between 0.8 rad/s and 1.4 rad/s, the heave-added mass per unit length decreases with increasing body length before all curves converge at the highest wave frequencies. A similar trend is observed for radiation wave damping, which has a nonlinear growth with increasing body length at the low and intermediate wave frequencies before converging at the highest plotted frequencies. The heave excitation force magnitude, $|X_3|$, and phase ϕ_3 for both bodies are plotted in Figure 3. In Figure 3a, the wave-excitation force magnitude has been normalized by the heave hydrostatic restoring coefficient, while in Figure 3b the phase has been normalized by π. The heave-wave excitation magnitude for body 1 is always larger than body 2 because of shielding effects; however, this difference is reduced as the body length is increased. The heave hydrostatic restoring coefficient scales linearly with body length, and Figure 3a shows that although the dimensional heave-wave excitation force is greatest for the longest body length, the increase per unit length is significantly reduced. For each body length, the heave-wave excitation force drops to 0 at wave frequencies that correspond to wavelengths that are integer multiples of the body length, which also corresponds to the near-zero crossings of the wave-exciting force phase in Figure 3b.

Next, the diameter of each body was modeled at three additional sizes, in addition to the base case, with the body length kept constant at 25 m. The heave radiation added mass and wave damping are plotted in Figure 4, and the heave-wave excitation force magnitude and phase are plotted in Figure 5. Unlike with increasing body length, increasing the diameter results in a nonlinear reduction in the heave added mass and wave damping rel-

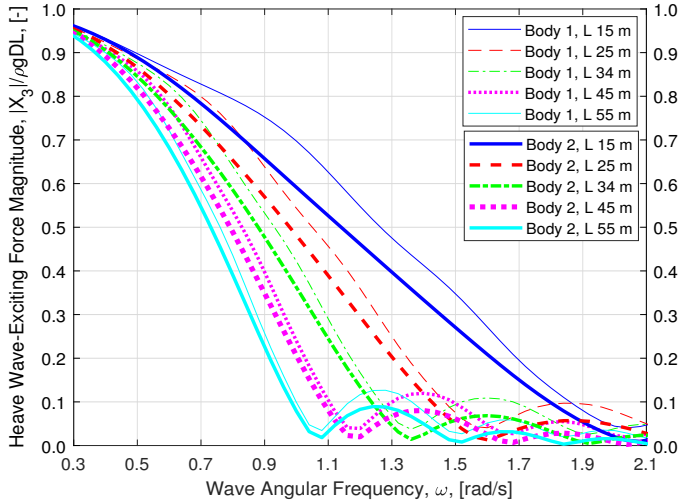

(a) Heave-Wave Excitation Force Magnitude $|X_3|$

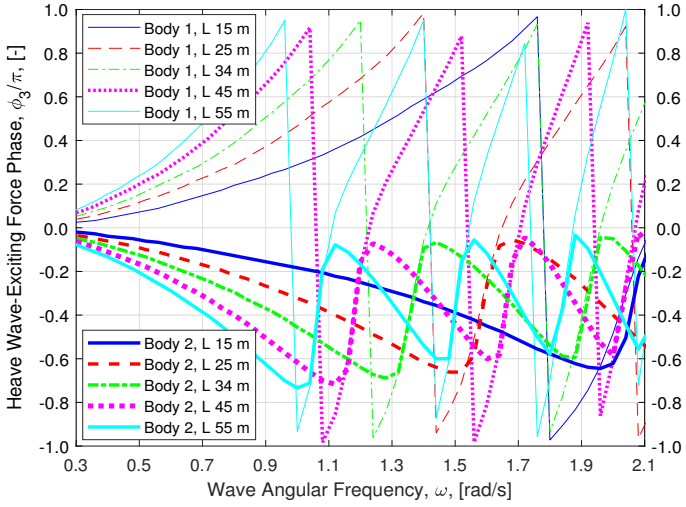

(b) Heave-Wave Excitation Force Phase ϕ_3

FIGURE 3. HEAVE-WAVE EXCITATION FORCE MAGNITUDE AND PHASE FOR BOTH BODIES AND EACH OF THE FIVE LENGTH CASES.

ative to the displaced volume of the body. The variation in the heave-wave excitation force magnitude with body diameter has a similar trend with increasing body length, where the excitation per unit width decreases as the diameter increases. Here, all body geometries have the minimum normalized heave excitation magnitudes at the same wave frequencies because the body length is constant.

WEC-SIM OPEN-SOURCE CODE

The power performance modeling for the attenuator WEC was completed in the open-source code WEC-Sim, which is jointly developed by Sandia National Laboratories and the National Renewable Energy Laboratory, through funding from the U.S. Department of Energy's Water Power Technologies Office [16]. The WEC-Sim code is developed in the MATLAB/Simulink environment and uses Simscape Multibody to solve for the WEC rigid body dynamics. WEC-Sim is a wave energy converter simulator that models the interaction between incident waves, device motion, PTO mechanism, and mooring structures. To solve for the WEC dynamic response, WEC-Sim uses the time-domain convolution integral formulation based on the Cummins equation [16].

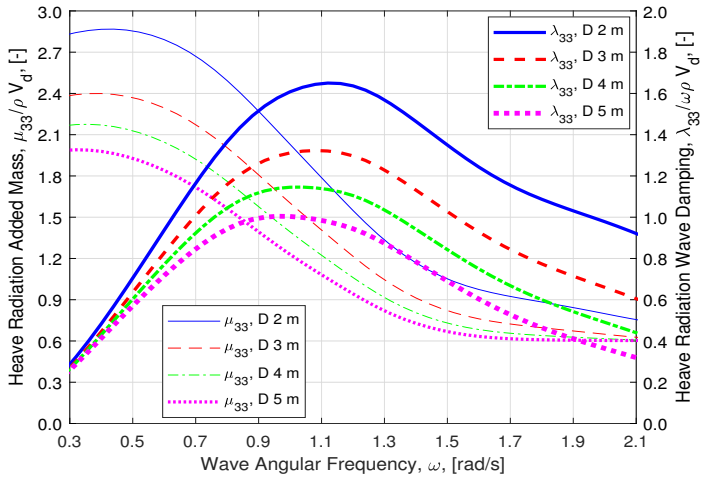

FIGURE 4. HEAVE RADIATION ADDED MASS, μ_{33}, AND WAVE DAMPING, λ_{33}, FOR EACH BODY 1 DIAMETER. BECAUSE THE RADIATION PROBLEM IS SYMMETRIC, THE RADIATION COEFFICIENTS WILL BE THE SAME FOR BODY 2 AND ARE THEREFORE OMITTED.

For this analysis, the Wave Energy Prize (WEP) sea states were chosen to evaluate the power capture performance of the two-body fixed-geometry attenuator. The WEP sea states consist of six representative sea conditions that a WEC deployed along U.S. coasts would likely encounter [17]. Each sea state is defined by a significant wave height, H_s, peak wave period, T_p, and time-averaged wave power flux, P_w, as shown in Table 2, and is described by a Bretschneider spectrum [16].

PTO POWER AND TORQUE PERFORMANCE MODEL

The WEC PTO system transforms the absorbed mechanical energy of the device to electricity, making it an important contributor to the power performance of the device. For this analysis, the PTO damping coefficient, B_g, was optimized for each hull shape and sea state to maximize power capture. Because of the complexity of the coupled equations of motion for both bodies, an analytical optimal value of B_g was not derived but was obtained by completing a parameter sweep. And, because

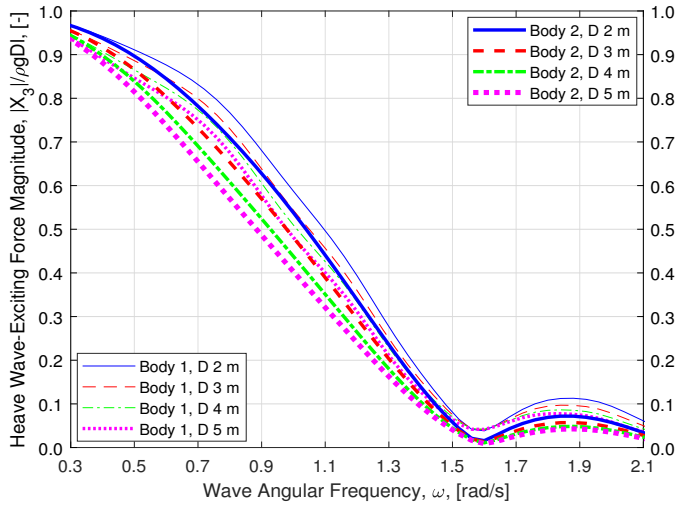

(a) Heave-Wave Excitation Force Magnitude $|X_3|$

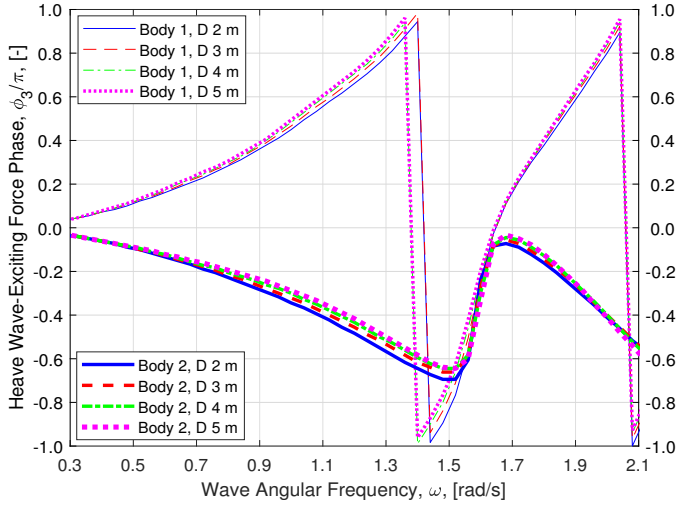

(b) Heave-Wave Excitation Force Phase ϕ_3

FIGURE 5. HEAVE-WAVE EXCITATION FORCE MAGNITUDE AND PHASE FOR BOTH BODIES AND EACH OF THE FOUR DIAMETER CASES.

the dynamic motion of the two bodies changes behavior with the incident wave characteristics, as well as the PTO damping coefficient, one would expect to see a change in the WEC's power capture with B_g, as shown in Figure 6. For this case, the time-averaged power capture follows a bell curve shape and peaks when the PTO damping coefficient is near 1^7 N·s·m/rad, while the PTO torque continues to increase with B_g.

The time-averaged power capture for each body length across each WEP sea state, has been plotted in Figure 7 and shows that the WEC with longer body units is capable of capturing greater power in sea states with the greatest wave steepness (Table 2). The corresponding PTO torque, plotted in Figure 8,

TABLE 2. WEP SEA STATES SIGNIFICANT WAVE HEIGHT, H_S, PEAK PERIOD, T_P, WAVE POWER FLUX, P_W, AND STEEPNESS.

Sea State	H_S [m]	T_P [s]	P_w [kW/m]	λ_{T_p}/H_s [-]
1	2.34	7.31	16.7	35.6
2	2.64	9.86	29.0	57.5
3	5.36	11.52	141.1	38.6
4	2.05	12.71	23.1	122.4
5	5.84	15.23	233.5	60.4
6	3.25	16.50	79.8	124.9

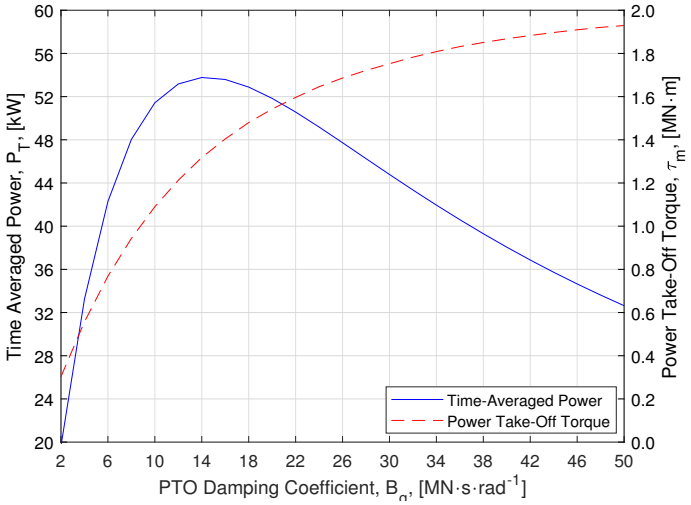

FIGURE 6. TIME-AVERAGED POWER CAPTURE (LEFT AXIS) AND PTO TORQUE (RIGHT AXIS) FOR THE TWO-BODY BASE MODEL IN WEP SEA STATE 3.

maintains a more even distribution across WEP sea states for the same body length case. The percentage change in PTO power capture and torque with body length, relative to the base case dimensions, is plotted in Figure 9 along with a linear scaling guideline as the structural mass increases linearly with body length. Figure 9 demonstrates that although the longer hull lengths have greater power capture, the increase in torque is much greater and thus drops further below the linear trend line. The results indicate that the device lengths between 25 m and 35 m have the best PTO power-to-torque ratio.

The effect of varying the hull diameter on the PTO time-averaged power and torque can be found in Figures 10 and 11, respectively, which indicate that larger diameters generate greater power, but also experience greater PTO torque. Similar to the analysis for varying hull length, Figure 12 plots the percent change in PTO time-averaged power against the percent change in PTO torque. Because increasing the body diameter results in a

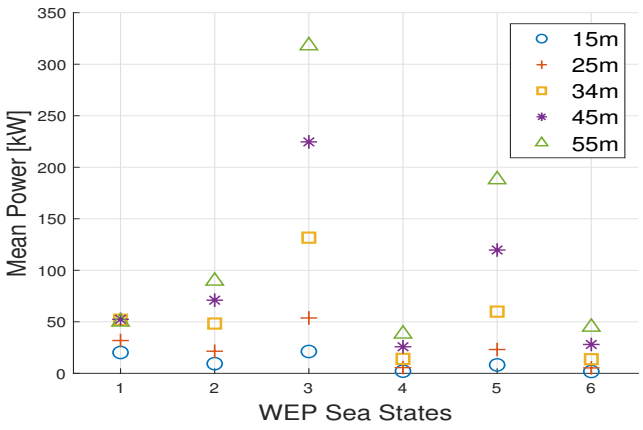

FIGURE 7. POWER COMPARISON ACROSS ALL WEP SEA STATES AND FOR EACH BODY LENGTH CASE.

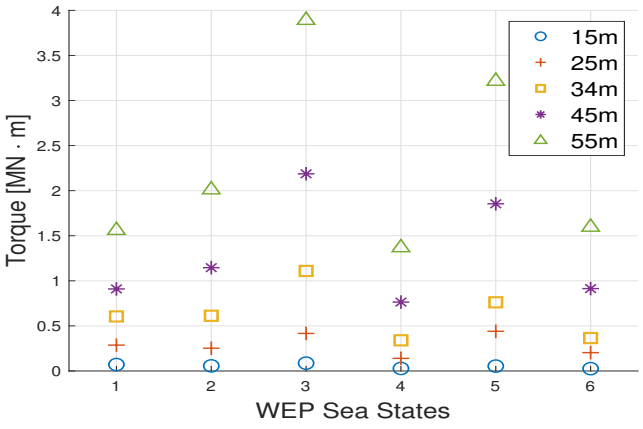

FIGURE 8. TORQUE COMPARISON ACROSS ALL WEP SEA STATES AND FOR EACH LENGTH CASE.

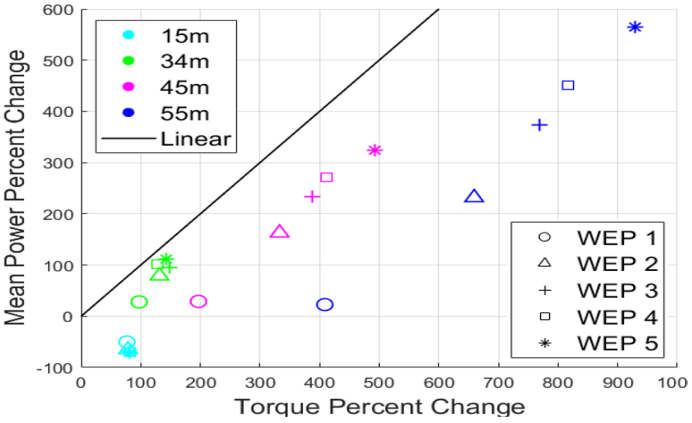

FIGURE 9. PERCENT CHANGE IN POWER CAPTURE AGAINST TORQUE FOR EACH LENGTH CASE AND ACROSS SELECT WEP SEA STATES.

quadratic increase in displaced mass, from a cost perspective the growth in time-averaged power and torque should lie on or above the quadratic scaling guideline shown in Figure 12. Points that appear below the quadratic indicate that either the PTO power capture has not increased as fast as—or the PTO torque has increased faster than—the hull displaced mass. If the PTO power capture lags the growth in hull mass, the developer will have to invest more in capital costs without receiving an equal return in power capture. Furthermore, even if the power capture follows the increase in displaced mass, if the PTO torque requirement increases much faster, the developer will be required to pay more for a larger-capacity PTO system and may also need to increase the structural steel thickness to ensure the hull-to-PTO connection does not fail. Therefore, the results from Figure 12 show that the likely optimum hull diameter will be between 2 m and 4 m and will have the best PTO power-to-torque ratio.

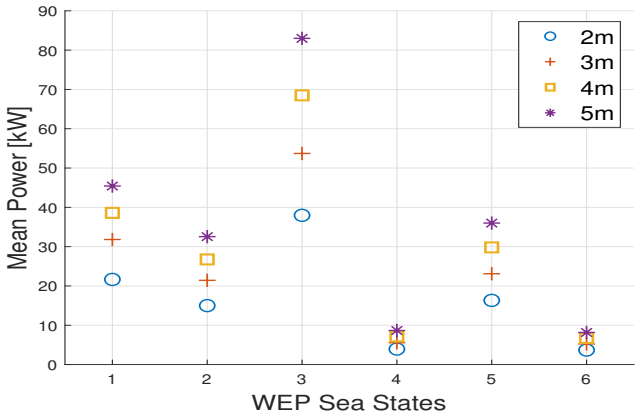

FIGURE 10. POWER COMPARISON ACROSS ALL WEP SEA STATES AND FOR EACH BODY DIAMETER CASE.

VARIABLE-GEOMETRY ATTENUATOR CONCEPT

The concept of incorporating variable-geometry components into the WEC structure remains a relatively unexplored research topic, with previous investigations considering a few sample WEC architectures. For example, variable-geometry modules were incorporated into the body of an oscillating surge WEC [18], and were successful at reducing both the PTO and structural loads on the device. For the analysis of a Pelamis-like attenuator, the variable-geometry modules consist of inflatable side bags or floats, as shown in Figure 13, that can inflate or deflate depending on sea conditions. In low-to-moderate seas, the bags would inflate in hope of increasing power capture, while in larger-to-extreme sea states the bags would be deflated to reduce hydrodynamic loading and allow the device to dive beneath the

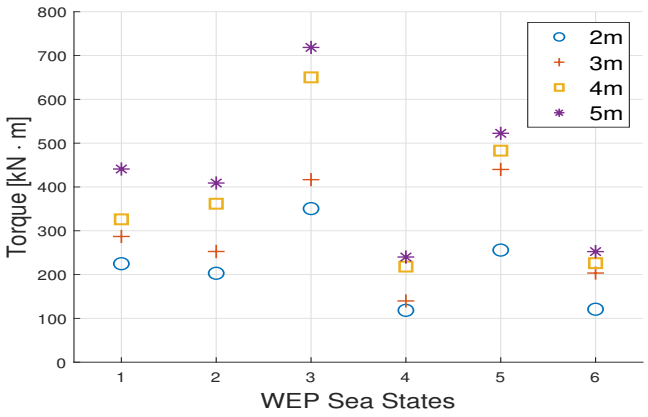

FIGURE 11. TORQUE COMPARISON ACROSS ALL WEP SEA STATES AND FOR EACH BODY DIAMETER CASE.

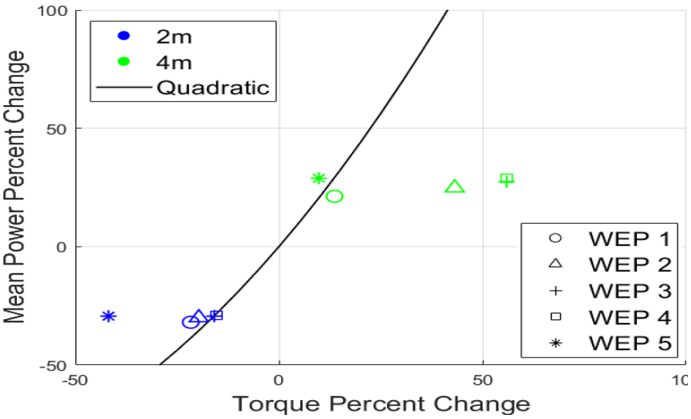

FIGURE 12. PERCENT CHANGE IN POWER CAPTURE AGAINST TORQUE FOR EACH DIAMETER CASE AND ACROSS SELECT WEP SEA STATES.

waves. The focus of this investigation was to characterize the effect of the variable-geometry modules in normal sea conditions, thus simulations were not completed in any extreme or survival sea states. The floats have been assumed to extend the full length on each side of the hull, along the x-axis, and are located on both body 1 and body 2. Each float is connected at the top of the hull, above water, and wraps around half of the circumference to the bottom where it meets the other float. When the floats are fully inflated, the cross section of the WEC hull becomes an ellipse because of the elongation of the width of the device along the y-axis. The elliptical cross section of the body section will be defined by a major axis, a, and minor axis, b. The hypothesis was that the major axis, a, is the dominant parameter in defining the power capture and thus using the floats to increase the surface area at the calm water surface would help maintain maximum power performance. To test how the variable-geometry modules affected the WEC power absorption and PTO torque, the major axis was kept constant, whereas the minor axis, starting at the same length as the major axis, was reduced by a factor of 3/4, 1/2, and 1/4 to create a set of four cases. A diagram of the different aspect ratios are shown in Figure 14. From the fixed-geometry analysis, the optimal fixed-geometry diameter lies in the 2 m to 4 m range, thus the lengths of a considered were 2 m, 3 m, 4 m, and 5 m.

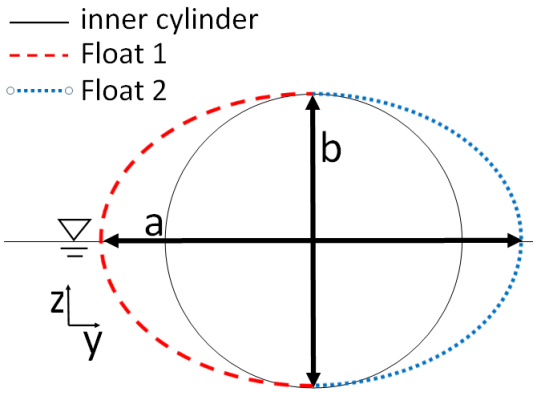

FIGURE 13. SCHEMATIC OF THE WEC CROSS SECTION, INCLUDING VARIABLE-GEOMETRY MODULES. THE INNER CYLINDER DIAMETER CORRESPONDS TO MINOR AXIS, B, WHILE THE FLOATS EXTEND TO MAJOR AXIS, A. EACH FLOAT COVERS HALF OF THE INNER CYLINDER'S CIRCUMFERENCE.

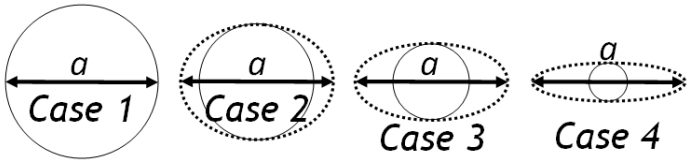

FIGURE 14. CASES 1-4 FOR A GIVEN MAJOR AXIS LENGTH, A. MINOR AXIS IS EQUAL TO THE MAJOR AXIS IN CASE 1, $\frac{3}{4}$ OF THE MAJOR AXIS FOR CASE 2, $\frac{1}{2}$ OF THE MAJOR AXIS FOR CASE 3, AND $\frac{1}{4}$ OF THE MAJOR AXIS FOR CASE 4.

Effect of Variable Geometry on Hull Hydrodynamics

For hydrodynamic modeling purposes, the inflatable bags have been assumed to withstand the required air pressure to maintain the idealized elliptical shape. The shape would more likely take on an inverted curved shape that would be dependent on the internal pressure, surrounding hydrostatic pressure, and

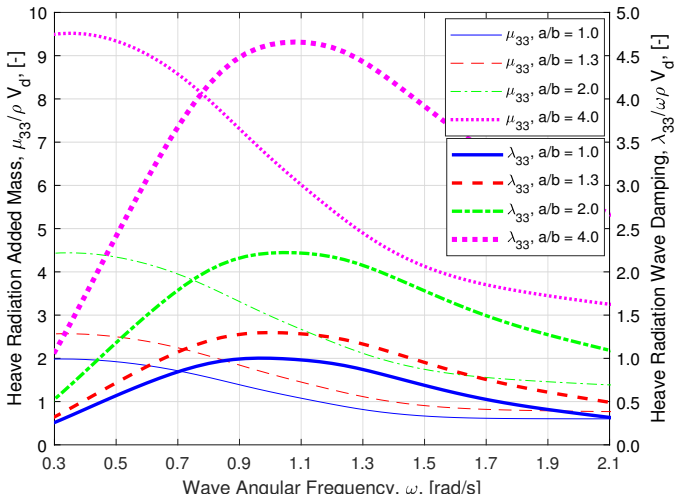

FIGURE 15. HEAVE RADIATION ADDED MASS, μ_{33}, AND WAVE DAMPING, λ_{33}, FOR ALL FOUR VARIABLE-GEOMETRY CASES WITH A 5-M MAJOR AXIS FOR BODY 1. BECAUSE THE RADIATION PROBLEM IS SYMMETRIC, THE RADIATION COEFFICIENTS WILL BE THE SAME FOR BODY 2 AND ARE THEREFORE OMITTED.

material stiffness of the bags. However, as a first step at understanding the changing hydrodynamics with WEC shape, the idealized shape is still valuable in understanding the potential of this novel feature. Figure 15 plots the heave radiation added mass and wave damping, nondimensionalized by the displaced fluid mass, for the variable-geometry aspect ratio cases 1-4, with a major axis length of 5 m. Increasing the aspect ratio increases both the nondimensionalized heave radiation coefficients; however, because the WEC displaced volume is also reduced with increasing aspect ratio, the dimensional added mass is smaller. Therefore, decreasing the aspect ratio to become more circular does not lead to increases in the hydrodynamics as compared to gains in the mass properties. As the minor axis decreases, the heave-wave excitation force magnitude at each wave frequency increases slightly, with almost no change in phase (Figure 16). While the wave-excitation force on body 2 starts at nearly the same magnitude as body 1, the excitation force quickly reduces, leading to a maximum reduction of roughly 20%-30% between wave frequencies 0.7 rad/s and 1.1 rad/s. The resulting heave-wave excitation force coefficients with increasing aspect ratio demonstrate that structural costs can be saved by reducing the WEC draft while maintaining nearly the same wave-excitation magnitude.

The second set of hydrodynamic results provided in Figure 17 plot the heave radiation coefficients with varying major axis lengths for case 4. Because the major-to-minor axis ratio remains the same, the change in hydrodynamics is coming from the size of the device rather than the elliptical shape. For each 1-m decrease in the major axis, the added mass drops by roughly 30%; however, the displaced volume decreases at a faster rate and thus the nondimensional radiation coefficients increase with a smaller major axis. The heave-wave excitation forces, shown in Fig. 18, decrease anywhere from 20% to 50% for each 1-m reduction in the major axis in the lower wave frequency range. But when the heave-wave excitation force is normalized by the heave restoring coefficient, which scales with the water plane area, the normalized values increase as the major axis is reduced, implying the reduction in the heave-wave excitation force scales nonlinearly with the major axis. As the wave frequency increases, the excitation force magnitudes for each case begin to converge toward one another until reaching the wave frequency that results in a wavelength nearly equal to the body length.

ACE CALCULATIONS

The performance values used to compare the fixed- and variable-geometry attenuator WECs are the average climate capture width (ACCW), the characteristic capital expenditure (CCE), and the ACE metrics that were established for the WEP [13]. The ACCW is a measure of the power capture efficiency of a WEC. It is defined as the weighted average of the mechanical absorbed power across multiple sea states, divided by the incident wave energy flux per meter crest width, C_P, as shown in the following equation:

$$ACCW_j = \frac{\sum_{i=1}^{n} \Xi_{ij} \langle AP(i) \rangle}{\langle C_P(j) \rangle} \tag{4}$$

where n is the number of sea states; Ξ_{ij} is the scaling factor for sea states, i, at each location j; $\langle AP(i) \rangle$ is the average mechanical power absorbed by the WEC for each sea state, i; and $\langle C_P(j) \rangle$ is the incident average annual wave energy flux for site j. The seven sites and associated scaling factors used in the WEP are shown in Table 3 [13].

The CCE is an estimate of the capital cost required to build the WEC hull, but does not include other costs with balance of system, such as mooring lines or PTO. The attenuator model is considered to be at a low technology readiness level (TRL), meaning the PTO systems, mooring lines, power cables, energy storage devices, and other nonload-bearing components are too variable in cost to estimate the LCOE at this stage of development. Operations and maintenance costs are also not included because they are difficult to estimate due to the limited availability of deployment data. The CCE is defined as the cost to buy the raw material and manufacture the load-bearing structure of the device, which is calculated from the following formula:

$$CCE = \sum_{k=1}^{N} m_k \cdot MMC_k \tag{5}$$

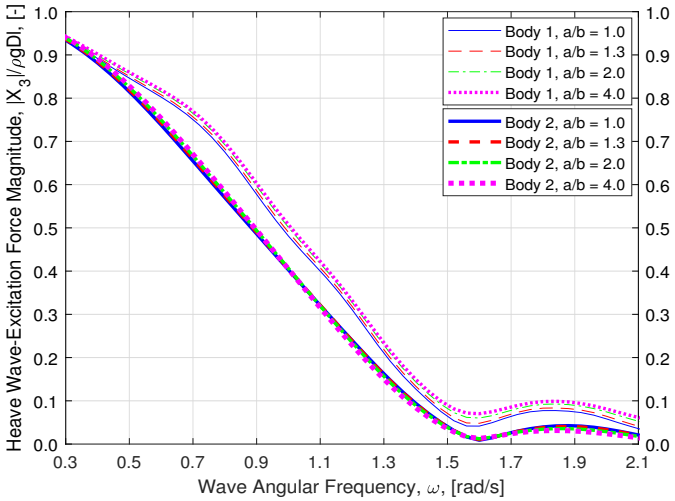

(a) Heave-Wave Excitation Force Magnitude $|X_3|$

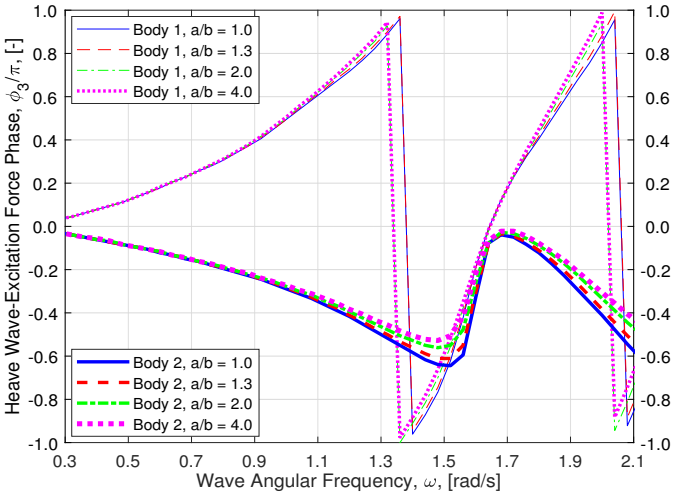

(b) Heave-Wave Excitation Force Phase ϕ_3

FIGURE 16. HEAVE-WAVE EXCITATION FORCE MAGNITUDE AND PHASE FOR BOTH BODIES AND EACH OF THE VARIABLE-GEOMETRY ASPECT RATIOS WITH A 5-M MAJOR AXIS.

where k is the material index, N denotes the number of key structural materials, m_k is the total mass of material k, and MMC_k is the manufactured material cost per unit mass of material k. The MMC_k values used in this study are shown in Table 4 [13]. Each hull geometry has a draft equal to half the diameter, meaning it sits halfway in the water. For a floating body to maintain this position relative to the still water line, the mass of the device must be equal to that of the displaced fluid water. The mass of Steel-A36 for each device was set equal to the mass of displaced water from the inner cylinder only.

The ACE metric is obtained by dividing the ACCW by CCE, $ACE = \frac{ACCW}{CCE}$, and is a cost-to-benefit ratio that primarily expresses the power absorption efficiency to the capital cost of building the device. The ACE metric was developed for the WEP competition to evaluate low TRL devices at the initial development stage. ACE does not take into account the power conversion losses, PTO loads, fatigue damage, or the costs of any items beyond the building of the WEC hull.

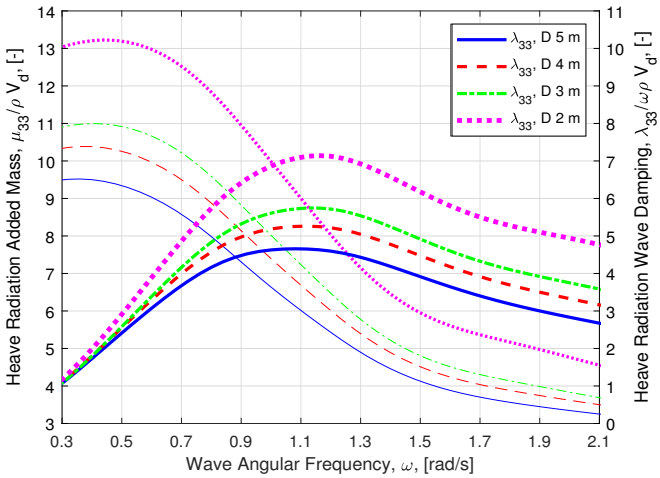

FIGURE 17. HEAVE RADIATION ADDED MASS, μ_{33}, AND WAVE DAMPING, λ_{33}, FOR VARIABLE-GEOMETRY CASE 4 WITH VARYING MAJOR AXIS LENGTH.

TABLE 3. SCALING FACTORS, Ξ_{IJ}, FOR EACH OF THE SEVEN U.S. SITES USED FOR EVALUATION OF THE ATTENUATOR WEC WRITTEN AS PERCENTAGES.

Site Location	SS1	SS2	SS3	SS4	SS5	SS6
Alaska	24.3	33.2	7.5	20.0	2.4	1.2
Washington	13.7	27.7	4.1	33.8	2.2	4.5
North Oregon	15.5	30.7	5.6	34.4	3.7	4.2
Oregon	17.5	26.8	5.8	29.5	3.4	5.4
North California	20.7	23.0	1.2	46.6	1.6	6.4
South California	15.2	27.0	1.4	39.1	1.0	9.5
Hawaii	32.8	24.5	0.1	13.3	0.0	1.3

TABLE 4. MANUFACTURED MATERIAL COST (MMC) OF THE KEY STRUCTURAL MATERIALS COMPOSING THE HULL.

Material, k	MMC_k [$/kg]	Density, ρ_k, [kg/m^3]
Steel-A36	3.00	7850
Coated Fabric	9.50	1400

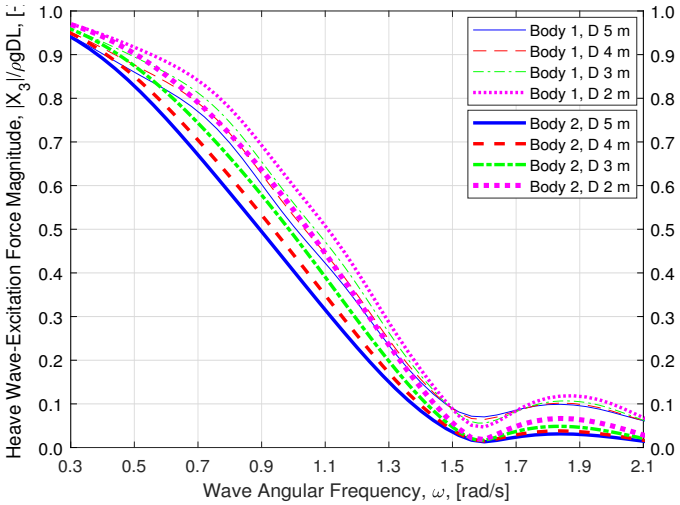

(a) Heave-Wave Excitation Force Magnitude $|X_3|$

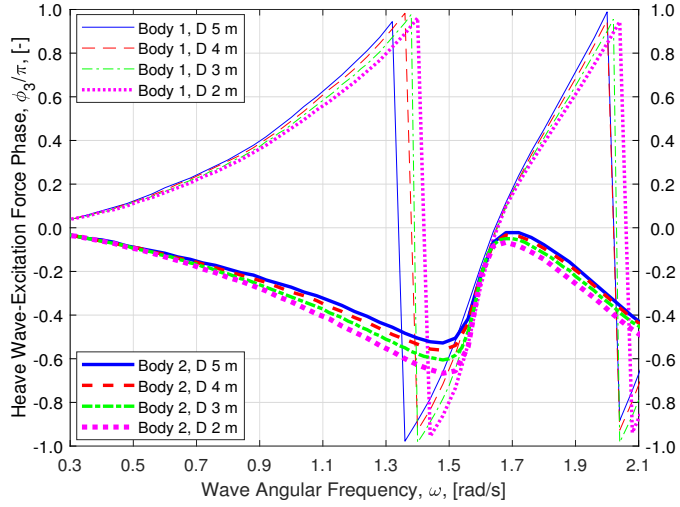

(b) Heave-Wave Excitation Force Phase ϕ_3

FIGURE 18. HEAVE-WAVE EXCITATION FORCE MAGNITUDE AND PHASE FOR BOTH BODIES FOR THE VARIABLE-GEOMETRY ASPECT RATIO EQUAL TO 4 WITH VARYING MAJOR AXIS.

Variable-Geometry ACCW, CCE, ACE, and PTO Torque

Case 1 for each major axis has no variable-geometry modules, thus the mass of the displaced water equals the total steel mass of the device. For cases 2–4, for each major axis, the mass of the variable-geometry modules was calculated by multiplying the circumference of the ellipse by a 20-mm thickness and the body length, L = 25 m, to estimate the bag volume and was multiplied by a density of 1,400 kg/m^3 to estimate the bag mass. Given the inflatable bags have been assumed to be pressurized by air, the weight required to offset the additional buoyancy has been assumed to come from seawater ballast. As the extra weight is assumed to come from ballast water, which can be pumped in and out of ballast chambers, no additional cost has been added to the CCE. However, for case 4 with major axis, a, equal to 3 m, 4 m, and 5 m, the volume of ballast water required to meet the desired draft was more than the inner cylinder could accommodate. Therefore, the volumetric ballast water limits for each major axis have been marked by a red 'x' in Figure 19b.

The resulting ACCW and CCE for each geometric configuration has been plotted in Figure 19a, with the resulting ACE metric plotted in Figure 19b. The ACCW values in Figure 19a show how efficient each geometric configuration is at capturing the incident wave power. The resulting ACCW values are nearly the same for each set of a, which demonstrates the variable-geometry WECs are capturing nearly the same amount of wave power, while the structural mass and associated CCE are decreasing nonlinearly with aspect ratio. The results for ACCW provide evidence that the major axis is the dominant parameter that defines the power capture potential, and the variable-geometry components would be well-suited to maintain the planform area. The ACE metric compares the power capture efficiency to the structural capital costs and, as shown in Figure 19b, the ACE metric increases with the aspect ratio, a/b. In addition, the ACE metric also has a step increase when decreasing the major axis of the elliptical body; however, because the power output decreases with the major axis length (Figure 19a), the only way to have an increase in ACE is to have a greater reduction in CCE. But, because ACE only considers up-front capital costs, the perceived gains from having multiple smaller units may be counteracted by larger operational and maintenance costs when compared to having only one or two larger units. The weighted average PTO torque, across the WEP sea states, is shown in Figure 20. Similar to the ACCW, the average PTO torque stays fairly constant across the aspect ratios for each major axis; however, the PTO torque is significantly greater for a = 5 m, and no explanation has yet to be identified by the authors. Overall, the results do imply that the variable-geometry cases could potentially provide the same power capture efficiency as fixed bodies with reduced capital costs.

CONCLUSIONS

The authors investigated a novel WEC device concept that combined an attenuator WEC with variable-geometry modules. The variable-geometry modules consisted of two identical inflatable bags, or floats, that spanned the length of each body and could inflate or deflate to change the device water plane area. The variable-geometry floats were shown to provide greater control over the device hydrodynamics that can be used to emphasize either power absorption or load shedding. However, the shape of the variable-geometry floats was modeled using rigid body hydrodynamics with an idealized shape, and further research is required to determine the flexibility of the

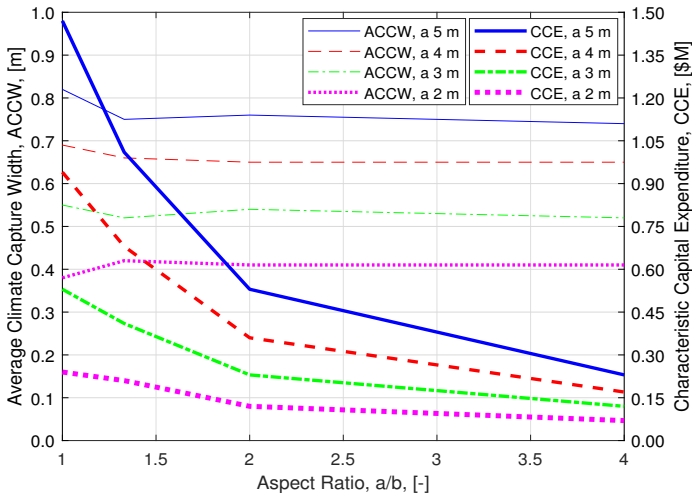

(a) Average Climate Capture Width, *ACCW*, and Characteristic Capital Expenditure, *CCE*

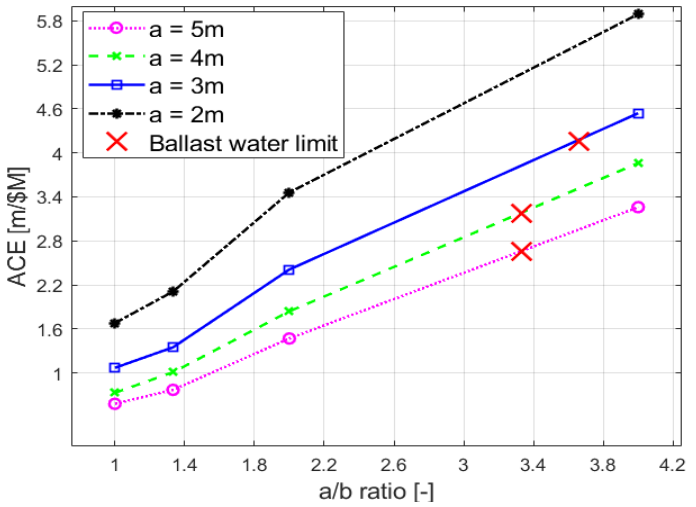

(b) ACE Metric Value

FIGURE 19. THE ACCW, CCE, AND ACE METRICS FOR EACH LENGTH OF A AND ASPECT RATIO A/B.

bag material, final submerged shape, and the influence of the flexible bag deformation on the dynamic response of the internal rigid body. The authors expect that improved control over the operational design loads, provided by the variable-geometry modules, has the potential to improve the capacity factor of the device in larger sea states. The current analysis has investigated device performance only in the irregular waves defined by the WEP, but additional optimization will be required under a site-specific joint probability distribution function and survival sea states. Furthermore, the PTO was modeled as a simple passive linear damper, but power capture could be further improved if a more advanced control strategy and PTO combination was utilized—one that allows for bidirectional energy flow. Future

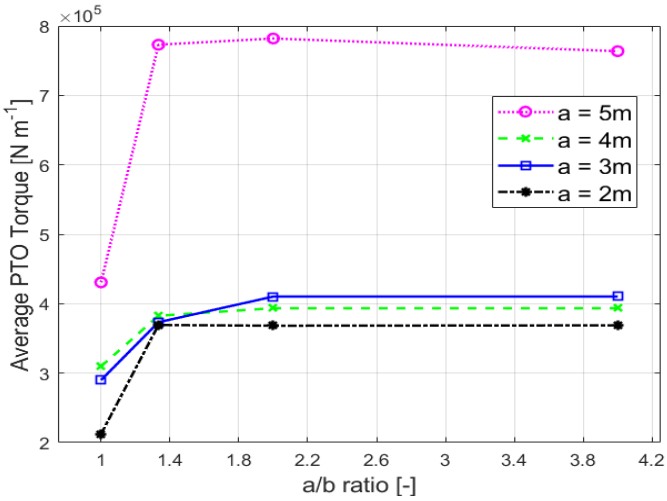

FIGURE 20. WEIGHTED AVERAGE PTO TORQUE FOR EACH LENGTH OF A AND ASPECT RATIO A/B.

work remains to evaluate the structural and actuator requirements to determine if the variable-geometry module design can be effectively controlled without adding significant capital and operational costs that would result in a minimal reduction in the LCOE.

ACKNOWLEDGMENT

This work was authored by the National Renewable Energy Laboratory, operated by Alliance for Sustainable Energy, LLC, for the U.S. Department of Energy (DOE) under Contract No. DE-AC36-08GO28308. Funding provided by the U.S. Department of Energy Office of Energy Efficiency and Renewable Energy Water Power Technologies Office. The views expressed in the article do not necessarily represent the views of the DOE or the U.S. Government. The U.S. Government retains and the publisher, by accepting the article for publication, acknowledges that the U.S. Government retains a nonexclusive, paid-up, irrevocable, worldwide license to publish or reproduce the published form of this work, or allow others to do so, for U.S. Government purposes.

REFERENCES

[1] Bull, D. and Ochs, M. E., 2013, "Technological cost-reduction pathways for attenuator wave energy converters in the marine hydrokinetic environment," Sandia National Laboratories SAND2013-7207.

[2] Drew, B., Plummer, A. R., and Sahinkaya,M. N., 2016, "A review of wave energy converter technology, Proceedings of the Institution of Mechanical Engineers, Part A: Journal of Power and Energy, 223 (8), 887-902.

[3] Weber, J.W. and Laird, D.L., 2015, "Structured innovation of high perfor-

mance wave energy converter technology," Proceedings of the 11th European Wave and Tidal Energy Conference, Nantes, France, Sept. 6–11.

[4] Neary, V., Previsic, M., Jepsen, R., Lawson, M. J., Yu, Y.-H., Copping, A., Fontaine, A., Hallett, K., Murray, D., 2014, "Methodology for design and economic analysis of marine energy conversion," Sandia National Laboratories SAND2013-7241.

[5] Jenne, D.S., Yu, Y.-H., Neary, V., 2015, "Levelized cost of energy analysis of marine and hydrokinetric reference models," Proceedings of the 3rd Marine Energy Technology Symposium, Washington, D.C., USA, April 27–29.

[6] Choiniere, M., Tom, N. M., and Thiagarajan, K. P., 2019, "Load shedding characteristics of an oscillating surge wave energy converter," Ocean Engineering, 186, pp. 105982.

[7] Yemm, R., Pizer, D., Retzler, C., and Henderson, R., 2012, "Pelamis: experience from concept to connection," Philosophical Transactions of the Royal. Society A, 370, pp. 365–380.

[8] Crestwing, 2020, "The prototype-Tordenskiold," last modified October 16, 2019, accessed January 13, 2020, https://crestwing.dk/english-2/tordenskiold-2.html.

[9] Zanuttigh, B., Angelelli, E., Castagnetti, M., Kofoed, J. P., Martinelli, L., and Clausen, L., 2011, "The wave field around DEXA devices and implications for coastal protection," Proceedings of the 9th European Wave and Tidal Energy Conference, Southampton, United Kingdom, Sept. 5–9.

[10] McNatt, J.C. and Retzler, C.H., 2019, "The performance of the Mocean M100 wave energy converter described through numerical and physical modelling," Proceedings of the 13th European Wave and Tidal Energy Conference, Naples, Italy, Sept. 1–6.

[11] Quocent, 2017, "Marine automatically stowable & inflatable volume (MASIV)," Wave Energy Scotland Novel Wave Energy Converter Stage 1 Project Public Report NW11_QUO_WES Public Report.

[12] Greaves, D., Hann, M., Kurniwan, A., Chaplin, J., and Farley, F., 2016, "The hydrodynamics of air-filled bags for wave energy conversion," Proceedings of the International Conference on Offshore Renewable Energy, Glasgow, Scotland, Sept. 12–14.

[13] Driscoll, F., Weber, J., Jenne, S., Thresher, R., Fingersh, L.J., Bull, D., Dallman, A., Gunawan, B., Ruehl, K., Newborn, D., Quintero, M., Labonte, A., Karwat, D., and Beatty, S., 2018, "Methodology to calculate the ACE and HPQ metrics used in the Wave Energy Prize," National Renewable Energy Laboratory NREL/TP-5000-70592.

[14] Gobato, R., Gobato, A., and Fedrigo, D. F. G., 2015, "Study Pelamis system to capture energy of ocean wave," last modified December 16, 2019, accessed January 12, 2020, https://arxiv.org/pdf/1508.01106.pdf.

[15] WAMIT, 2019, "Version 7.3 User Manual," accessed January 12, 2020, https://www.wamit.com/manual.htm.

[16] Yu, Y.-H., Lawson, M., Ruehl, K., and Michelen, C., 2014, "Development and Demonstration of the WEC-Sim Wave Energy Converter Simulation Tool, Proceedings of the 2nd Marine Energy Technology Symposium, Seattle, WA, April 15–18.

[17] Bull, D., and Dallman, A., 2017, "Wave energy prize experimental sea state selection," Proceedings of the 36th International Conference on Ocean, Offshore and Arctic Engineering, Trondheim, Norway, June 25–30.

[18] Kelly, M., Tom, N M., Yu, Y.-H., and Thresher, R., 2017, "Development of the second-generation oscillating surge wave energy converter with variable geometry," Proceedings of the 27th International Ocean and Polar Engineering Conference, San Francisco, California, USA, June 25-30.